ACS Photonics

pubs.acs.org/journal/apchd5

Article

Supercontinuum Generation in High Order Waveguide Mode with near-Visible Pumping Using Aluminum Nitride Waveguides

Hong Chen, Jingan Zhou, Dongying Li, Dongyu Chen, Abhinav K. Vinod, Houqiang Fu, Xuanqi Huang, Tsung-Han Yang, Jossue A. Montes, Kai Fu, Chen Yang, Cun-Zheng Ning, Chee Wei Wong, Andrea M. Armani,* and Yuji Zhao*

Cite This: *ACS Photonics* 2021, 8, 1344−1352

Read Online

ACCESS | Metrics & More | Article Recommendations | Supporting Information

ABSTRACT: Optical sources emitting in the ultraviolet (UV) to near-infrared wavelength range are an enabling tools for a wide variety of applications. To achieve broadband coherent generation within visible and UV spectrum, one fundamental obstacle is the strong material dispersion which limits efficient frequency conversion. Previous works have addressed this challenge by either using high input energies or delicate resonant structures. In this work, a simple device system is proposed to tackle the problem. Single crystalline aluminum nitride material with a threading dislocation density less than 10^9 cm^{-2} was used to provide broadband transparency, and a high order waveguide mode (transverse electric, TE_{10}) was used to create anomalous dispersion near 800 nm, in which soliton fission processes are supported. As a result, supercontinuum generation from 490 nm to over 1100 nm with a second harmonic generated band covering from 407 to 425 nm is achieved with the total on-chip pulse energy of 0.6 nJ.

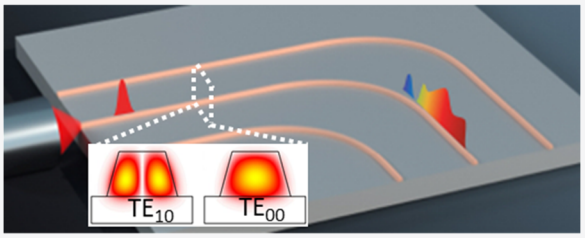

KEYWORDS: *aluminum nitride, nonlinear optics, supercontinuum generation, soliton dynamics, second harmonic generation, nonlinear Schrödinger equation*

On-chip supercontinuum generation spanning from ultraviolet (UV) through infrared (IR) with low (sub-nJ) powers has been a quest of researchers since the original demonstration of the laser in the 1960s.[1,2] An integrated system would enable research efforts and technology in coherent white light emitters,[3,4] frequency metrology,[5,6] and imaging.[7,8] While attempts have been made using a wide range of material systems and nonlinear phenomena,[9−19] this goal has so far eluded the research community due to fundamental principles. Namely, the majority of attempts relied on a combination of self-phase modulation (SPM) and soliton dynamics where the solitons were launched deeply inside the anomalous dispersive region[10,12] in fundamental transverse electric (TE) or transverse magnetic (TM) modes. Moreover, most of the boradband supercontinuum generation relies on the soliton dynamics in fundamental waveguide mode, with the pumping wavelength located in infrared wavelengths,[9−13,16,19,20] including a recent publication,[21] where visible to mid-infrared supercontinuum generation was demonstrated using AlN waveguide with second/third harmonic generated spectra in UV and visible range. Due to the increasing research interests in UV−visible spectrum for quantum optical science and biological sensing,[22,23] a near-visible wavelength pumped (or eventually visible wavelength pumped) supercontinuum generator is on demand for better spectral efficiency. To realize this target, one of the barriers is the strong material dispersion that hindered the formation of anomalous dispersion.

To tackle this challenge, several nonlinear optical processes can be employed with both advantages and limitations. For example, SPM is the most commonly observed process in the initial stage of spectrum broadening, however, it requires extremely high excitation power to further expand the spectrum.[24] Four-wave mixing has also demonstrated broadband frequency generation.[25] However, it relies on high performance resonating structures to achieve the high optical intensities. Additionally, this approach has limited bandwidth due to the requirement of phase-matching.[17] Self-steepening has the potential for broadband supercontinuum generation in UV−visible range; however, it requires small and flat dispersion near pumping wavelengths to efficiently build the steep temporal structures.[14] This process is hindered by the strong material dispersion in the near-visible spectrum. Other nonlinear processes such as Raman scattering[26] and modu-

Received: November 22, 2020
Published: April 26, 2021

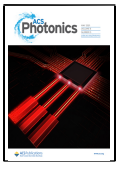

https://doi.org/10.1021/acsphotonics.0c01785
ACS Photonics 2021, 8, 1344−1352

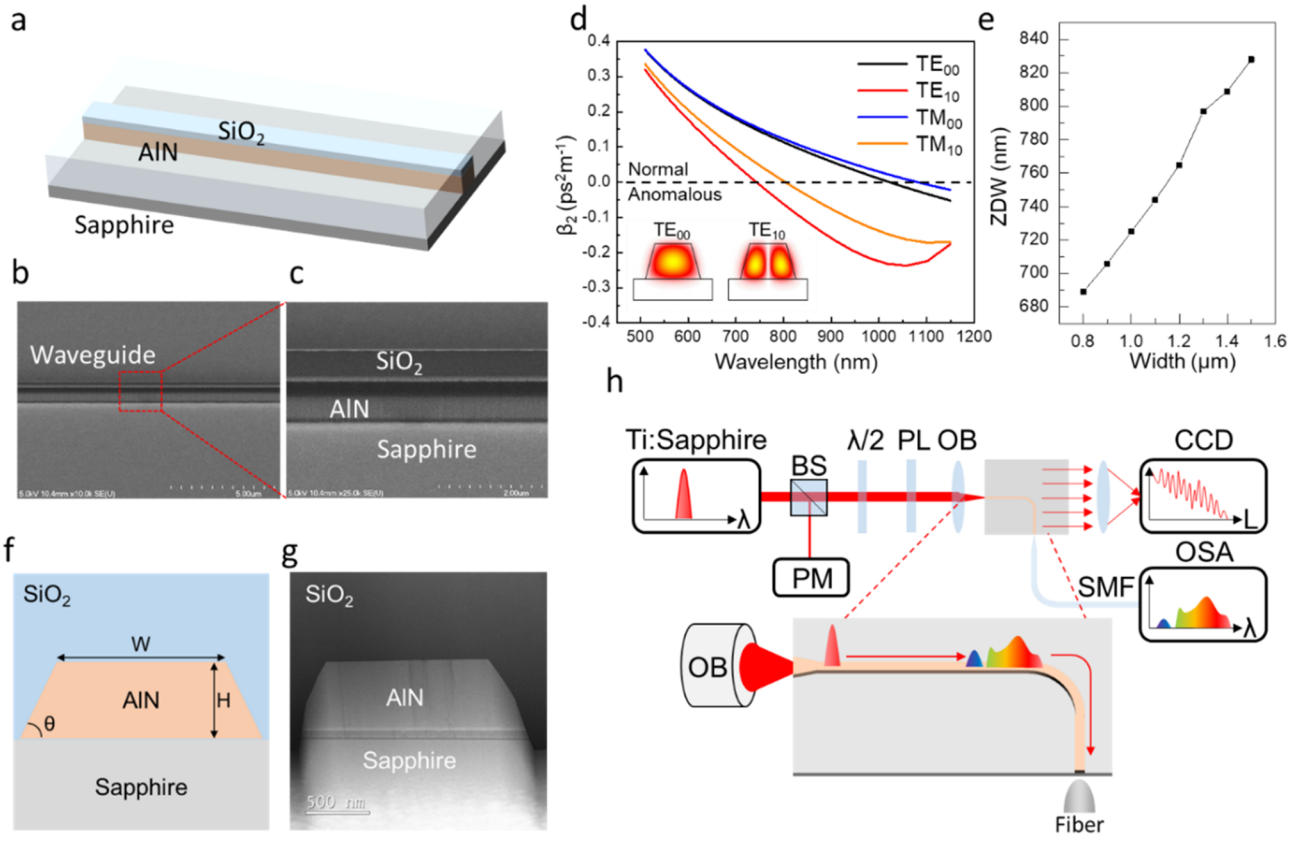

Figure 1. Device schematic, working principle, and design of experiment. (a) Three-dimensional schematic of the waveguide fabricated in this research. The coating and cladding layer is semitransparent for illustration purpose. (b) Tilted scanning electron microscope image of the AlN waveguides fabricated in this research, the orientation is similar to (a). Images were token before the deposition of coating layer. (c) Zoomed view of (b). The SiO_2 hardmask remains on top. Smooth sidewalls can be identified from the zoomed image. (d) Calculated GVDs of TE_{00}, TE_{10}, TM_{00}, and TM_{10} modes in a 1.1 μm × 1.2 μm ($W \times H$) AlN waveguide. The inset shows the mode profiles ($|E_x|$) of TE_{00} and TE_{10} modes, which are the modes that are used in this work. (e) The zero-dispersion wavelength increases as the width increases. The height was kept at 1.2 μm. (f) Cross section schematic view of the AlN waveguide, where the waveguide geometries such as width (W), height (H), and sidewall angle (θ) are defined. (g) Transmission electron microscope image of a typical AlN waveguide fabricated in this work. (h) Experimental setup implemented in this work. BS, $\lambda/2$, PL, PM, and OB indicate beam splitter, half-wavelength plate, polarizer, power meter, and optical objective lens, respectively.

lation instability[26] are usually accompanied by strong phase noise and thus are not favorable. A recent demonstration overcomed this challenging by utilizing the high $\chi^{(2)}$ of AlN with tapered waveguide structures.[17] This approach enabled broadband generation with a pulse energy of only 0.237 nJ. The spectrum ranged from approximately 650−900 nm with a second spectrum from approximately 350−450 nm. This wavelength range, and discontinuity, is due to the operation in the normal group velocity dispersion (GVD) regime. Therefore, it is a fundamental limit of the device design and operation.

To overcome these barriers, the present work demonstrates an approach, where a high order waveguide mode (TE_{10}) was selected to provide anormalous dispersion, which allows dispersive wave generation with near visible pumping. A broadband transparent AlN platform (Figure 1a−c) with dispersion engineered waveguides was used, and the supercontinuum generation from blue to near IR wavelengths with sub-nJ pulse energy was realized. To overcome the strong material dispersion, a high order waveguide mode (TE_{10}) was chosen. A convenient and high efficiency excitation strategy was used to achieve decent free-space to waveguide coupling efficiency. Additionally, the solitons were launched near the zero-dispersion wavelengths (ZDW), reducing the required pulse energy. Moreover, the metalorganic chemical vapor deposition (MOCVD) grown single crystalline AlN exhibited low threading dislocation density (less than 10^9 cm^{-2}), and as a result, relative low propagation losses were achieved at the pumping wavelengths.

EXPERIMENTAL DESIGN

To optimize the dispersion of the AlN waveguide, the modal dispersion for a series of waveguide geometries was computed from an in-house made numerical solver based on finite-difference method (FDM) provided in.[27] The computed dispersions were compared with commercial software (Lumerical) to confirm accuracy. These calculations were used to guide the device design and mode selection. For example, the calculated GVD in a 1.1 μm × 1.2 μm ($W \times H$) waveguide is shown in Figure 1d. Due to the highly dispersive material property, TE_{00} and TM_{00} modes exhibit normal dispersion below 1000 nm, while TE_{10} mode shows anomalous dispersion above 740 nm. Anomalous dispersion supports the formation of solitons near the operating wavelengths of Ti:sapphire laser. The ZDW of this TE_{10} mode is widely tunable by varying waveguide widths, as illustrated in Figure 1(e). To simulate the complete spectrum, the generalized multimode nonlinear Schrödinger equation (GMMNLS) was

https://doi.org/10.1021/acsphotonics.0c01785
ACS Photonics 2021, 8, 1344−1352

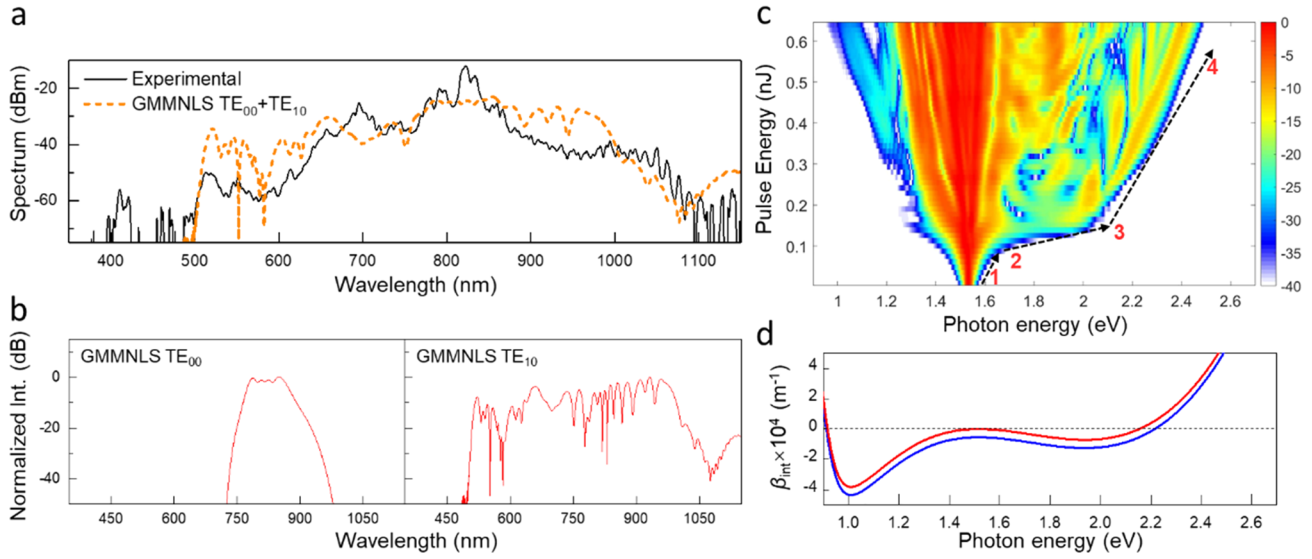

Figure 2. Experimental and modeling results of supercontinuum generation. (a) Experimental results of the supercontinuum spectrum (black solid) and the GMMNLS simulated spectrum involving TE_{00} and TE_{10} modes (orange dash) for the AlN waveguide. The spectrum is generated with a pump wavelength of 810 nm at average total on-chip power of 50 mW. (b) The normalized field intensity within TE_{00} and TE_{10} modes obtained from GMMNLS. The spectrum broadening is mainly due to the dispersive wave generation from TE_{10} mode. (c) Spectral evolutions of the AlN waveguide at different pulse energy from 0.01 to 0.64 nJ. From points 1−2, 2−3, and 3−4, the broadening mechanism was governed by SPM, DW generation, and optical power dependent phase-matching between soliton and DW. At each pulse energy, the spectrum is normalized to the maximum spectral intensity. (d) The integrated dispersion of TE_{10} mode vs photon energy at the optical power. The red and blue curves indicate the integrated dispersions with (red) and without (blue) the power-dependent term.

implemented. Details of the GMMNLS simulation is described in Methods.

While the theoretical metrics detailed in Figure 1d,e provide a general framework, previous experimental device efforts have shown that even nanometer scale roughness can significantly diminish an optical device performance.[28] As a result, the material deposition and fabrication procedures play a critical role in the device performance. To overcome this barrier, single crystalline AlN thin films were epitaxially grown by MOCVD on sapphire substrates. The growth was optimized to create films with a threading dislocation density less than 10^9 cm^{-2} identified by X-ray powder diffraction (XRD), resulting in broadband optical transparency. The surface roughness, as determined by atomic force microscopy (AFM) in a 5 μm × 5 μm scan, had a root mean squared (RMS) roughness of ∼3 nm. Refractive indexes of the thin films, as measured by ellipsometry at 800 nm, were 2.05. Original data on the material characterizations (XRD, AFM, ellipsometry) are provided in Figure S1.

Figure 1f shows the schematic cross-section of the device structure of the AlN waveguide, where the waveguide geometrical parameters, such as width (W), height (H), and sidewall angle (θ), are defined. SiO_2-clad waveguides were fabricated from 1.2 μm thick films (H) of AlN with widths ranging from 0.8 to 1.6 μm and lengths around 0.6 cm. After a propagation length of 0.6 cm, the waveguide was rotated by 90° and the light was collected by a lensed fiber. With this design, a large portion of stray light was avoided. Figure 1g shows a transmission electron micrograph (TEM) image of a representative cross-section of the AlN waveguide. The crystalline nature of the AlN thin film is clearly evident. Additional material data and waveguide fabrication details are in Methods.

The experimental setup is depicted in Figure 1h. A linearly polarized standard Ti:sapphire laser (Spectra Physics) with 100 fs pulse width (full-width half-maximum) and 82 MHz repetition rate was used. A beam sampler (1:99) and a thermal optical power sensor were utilized to monitor the optical power before chip. The average power in free space was tuned below 150 mW to avoid any damage to the sample. To couple light into the on-chip waveguides from the free-space laser, end-fire coupling was utilized. The out scattered light from the waveguides was collected by a linear CMOS camera (Thorlabs DCC1240) and used to perform propagation loss estimation. A tapered fiber was placed near the output port of waveguides, and the output signal was fed into optical spectrum analyzer (Yokogawa AQ6373B). Coupling strategies to efficiently excite the high order modes are discussed in Methods.

RESULTS AND DISCUSSIONS

A broadband supercontinuum spectrum is shown in Figure 2a. It is difficult to define the spectrum broadening from TE_{10} mode using conventional −20 or −30 dB criteria as the spectrum is consists of TE_{00} and TE_{10} mode, and the TE_{00} spectral component spans near the pumping wavelength due to its normal dispersion, while the TE_{10} mode is responsible for the spectrum broadening. The output signal spans from 490 to 1100 nm, which is over one octave. Due to the second order susceptibility of AlN, a secondary spectrum was observed from 407 to 425 nm. The pumping wavelength was slightly tuned near 800 nm, and the best spectrum (Figure 2a) was recorded at λ = 810 nm. Minor changes were observed when varying the pumping wavelength from 800 to 820 nm. According to the numerical simulation using coupled mode theory, the free-space to on-chip coupling efficiencies of TE_{00} and TE_{10} modes are 15% and 20%, respectively (Figure S4). Therefore, the on-chip average power used in Figure 2a can be estimated to be ∼50 mW (TE_{00} + TE_{10}); thus, the average power within TE_{10} mode was estimated to be ∼30 mW, corresponding to a pulse energy of 0.36 nJ. This pulse energy is among the lowest values

https://doi.org/10.1021/acsphotonics.0c01785
ACS Photonics 2021, 8, 1344−1352

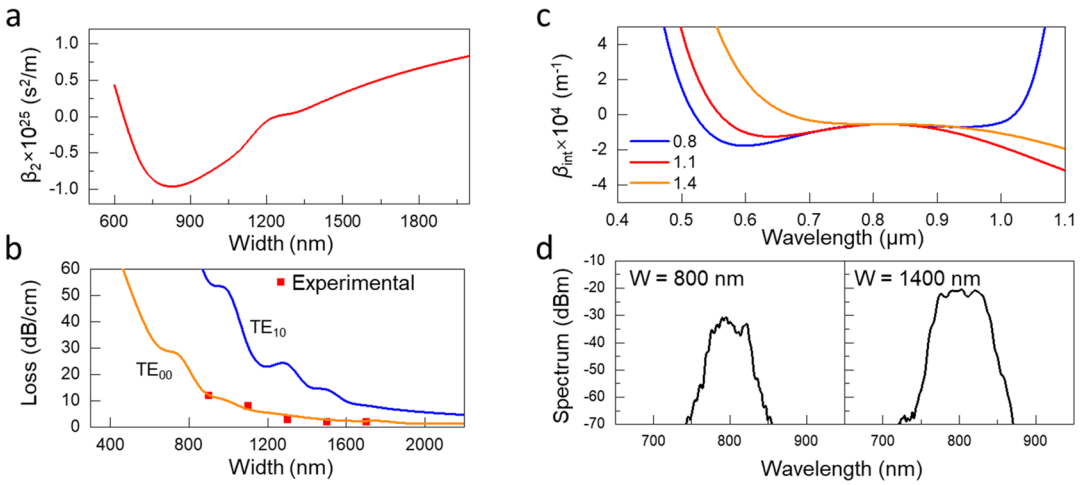

Figure 3. Experimental and modeling results of devices with different geometries. (a) The calculated GVD (β_2) for AlN waveguides. (b) Experimentally measured propagation loss (square points) in dB/cm at the wavelength of 800 nm, and the calculated propagation loss for TE_{00} (orange curve) and TE_{10} (blue curve) modes for AlN waveguides with different widths. (c) The calculated integrated dispersion vs wavelength for waveguide width at 0.8, 1.1, and 1.4 μm. (d) Measured spectrum in AlN waveguides with widths of 800 and 1400 nm. The spectrum was mainly broadened by SPM of the fundamental TE_{00} mode.

when compared with other supercontinuum generation methods at short wavelengths.[12,14,16]

The experimentally measured spectrum can be compared to the spectrum calculated using the GMMNLS (Figure 2a). The normalized field intensities of TE_{00} and TE_{10} modes are given separately by Figure 2b. As predicted in Figure 1c, the TE_{00} mode was propagating within the normal dispersion region. Therefore, SPM is the major contributor to its broadening mechanism. In contrast, for the TE_{10} mode, the pulse was split into its constituent fundamental solitons, and the solitons were phase matched to DWs in the short wavelengths. As a result, DWs emitted near 500 nm were achieved, enabling the formation of the broadband supercontinuum in the TE_{10} mode case. To validate the DW emission from high order mode, similar experiments were performed in coupled waveguide geometries, where only TE_{even} and TE_{odd} modes were supported, and the DW emission can still be identified as shown in Figure S7.

The discrepancy between experiment and GMMNLS can be mainly attributed to wavelength dependent propagation loss in TE_{10} mode. Under high power excitation, other physical processes might also take place such as thermal effects,[29] multiphoton absorption, free carrier absorption,[30] wavelength-dependent linear and nonlinear parameters,[31,32] and mode avoid-crossing,[33] making it hard to accurately predict the spectrum shape at all wavelengths. It should be noted that when the on-chip average power exceeds ~100 mW, behaviors indicative of thermal melting or dielectric breakdown began to be observed (Figure S3). Notably, irreversible material damage was occurred, inducing material defects that can be readily identified under the microscope via white light luminescence from defect states.[34] To avoid this irreversible damage, the on-chip power was kept at least two times lower than this value.

The spectrum versus pumping energy is investigated in Figure 2c. At low pulse energy, the spectral broadening is mainly governed by SPM (points 1 to 2). The spectrum can be asymmetrically expanded by DW emission when further increasing the pulse energy above 0.1 nJ (points 2 to 3). From points 3 to 4, blue shifts of DW can be observed, which can be attributed to the power-dependent phase matching condition for DWs:[26]

$$\beta(\omega) = \beta(\omega_s) + \beta_1(\omega - \omega_s) + \frac{1}{2}\gamma P_s \quad (1)$$

where β indicates the wavevector. ω_s and ω indicate angular frequency of soliton and DW, respectively. β_1 is equal to $\partial\beta/\partial\omega$. P_s is the power within soliton modes. γ is the nonlinear parameter that described by $(\omega n_2)/(cA_{eff})$, where the c and A_{eff} indicate vacuum speed of light and effective modal area, respectively. The blue shifts of DW with increasing power can be attributed to the power-dependent term in the eq 1.

The phase-matching between DW and soliton can be furthre revealed in Figure 2d, in which the integrated dispersion (eq 2) is employed to identify the spectral component:

$$\beta_{int}(\omega) = \beta(\omega) - \beta(\omega_s) - \beta_1(\omega - \omega_s) - \frac{1}{2}\gamma P \quad (2)$$

To investigate the geometry dependence of the process and create a generalizable waveguide design strategy, the GVD (β_2) for AlN waveguides with different widths is calculated (Figure 3a). Based on this graph, it is evident that a waveguide width below 1200 nm is required to support the solitons near the pumping wavelengths. It is also noteworthy that below a waveguide width of 800 nm, the waveguide loss increase expotentially, as shown in Figure 3b. When the waveguide width < 800 nm, the propagation loss of TE_{10} mode exceeds 60 dB/cm, the presence of strong loss prohibits the fission process. To further reveal the geometry dependence, the integrated dispersions at different geometries are given in Figure 3c.

Combining the observations in Figure 3a,b, the width of the AlN waveguide devices for this work is limited between ~1000 to ~1200 nm. To verify these calculations, devices outside of this optimum range were fabricated and characterized. Figure 3d illustrates the measured spectrum when pumping the waveguides with widths of 800 and 1400 nm. The broadening processes in these two waveguide designs can be clearly identified as SPM as a result from strong loss and normal dispersion, respectively.

https://doi.org/10.1021/acsphotonics.0c01785
ACS Photonics 2021, 8, 1344−1352

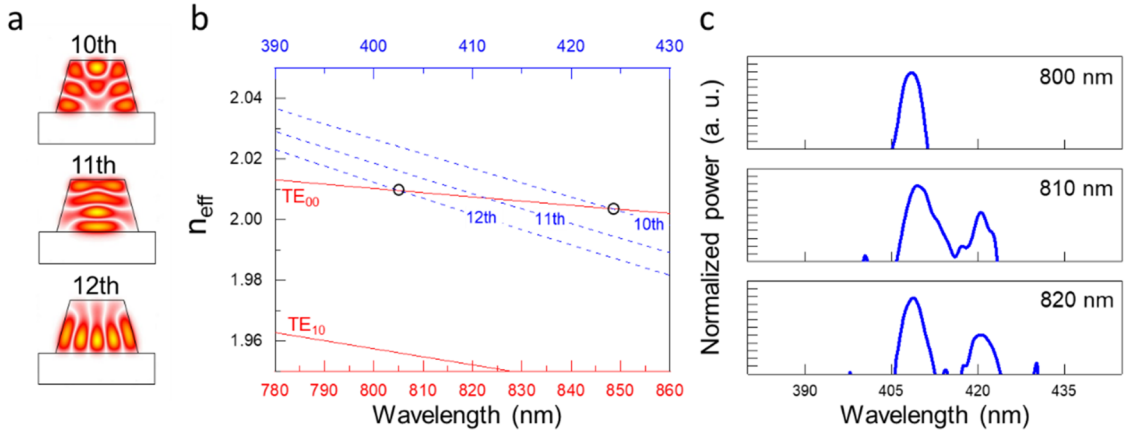

Figure 4. Experimental and modeling results showing the role of SHG. (a) Mode profile (E_y) of each high order mode computed at 400 nm wavelength. (b) The modal dispersion of the TE_{00} and TE_{10} modes near 800 nm (red curves) and the dispersion of several high order modes near 400 nm (blue dash curves) for the secondary spectrum from 407 to 425 nm in Figure 2a. Phase matching wavelengths can be determined at the crossing points of the curves. The two experimentally measured peaks can be identified near the two indicated points. (c) SHG signal near 400 nm at different pumping wavelengths. The locations of the SHG peaks were invariant to pumping wavelengths.

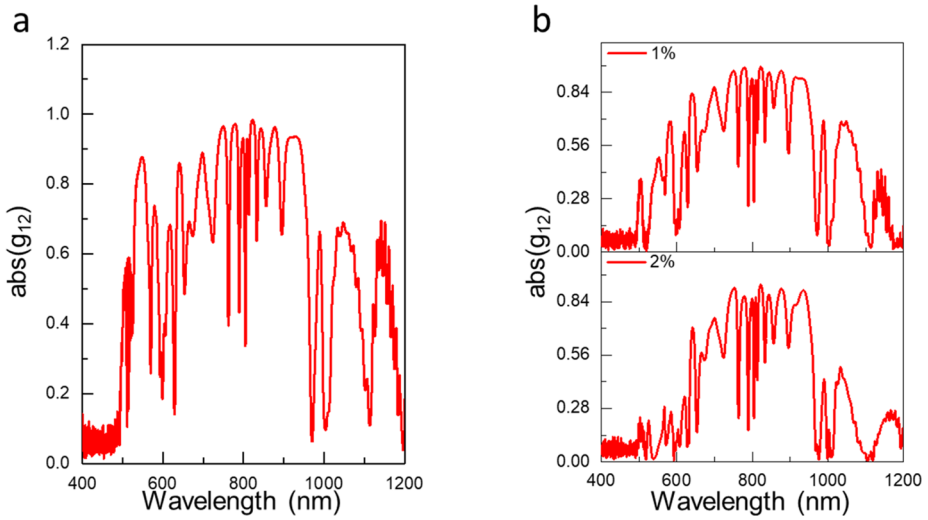

Figure 5. Simulated first-order coherence function for TE_{10} mode vs wavelengths for AlN waveguide with a width of 1.2 μm at different noise conditions. (a) The coherence function with quantum limited shot noise involved. (b) In addition to the shot noise, 1% (top) and 2% (bottom) RIN are involved.

While the generation of the primary spectrum from 490 to 1100 nm in the visible spectrum with only 0.36 nJ within TE_{10} mode is remarkable, the simultaneous generation of an even higher energy (lower wavelength) secondary spectrum spanning from 407 to 425 nm further increases the potential impact of this system. To understand the physical mechanism that gives rise to this secondary spectrum, we solve for the mode dispersion near the fundamental and the SHG wavelengths, and the mode profiles of high order modes near SHG wavelengths are depicted in Figure 4a. Since the pumping polarization is in TE, the SHG is relying on d_{31} of AlN. Figure 4b shows the modal dispersion of the TE_{00} and TE_{10} modes near 800 nm, and the dispersion of several high order modes near 400 nm. It can be observed that the TE_{00} mode is phase matched to three high order TM modes (10th−12th) within the range betwen 400 and 425 nm. Furthermore, Figure 4b also shows the dispersion curve of the TE_{10} mode in the near-visible region. Since the phase-matching point is far away from 400 nm, we neglect the SHG effect from the TE_{10} mode.

The normalized SHG efficiency can be described as[35]

$$\eta = \frac{8\pi^2}{\varepsilon_0 c n_1^2 n_2 \lambda^2} \frac{\zeta^2 d_{\text{eff}}^2}{A_{\text{eff}}} \tag{3}$$

where the ε_0 is the vacuum permittivity, c is the speed of light in vacuum, n_1 and n_2 are the refractive indexes at fundamental and second-harmonic wavelengths, respectively, A_{eff} represents the effective mode area, and d_{eff} represents the effective nonlinear susceptibility. The ζ indicates the spatial mode overlap factor, which can be given as[35]

$$\zeta = \frac{\int_{\chi^{(2)}} (E_{1y}^*)^2 E_{2y}\, dx\, dy}{\left|\int_{\chi^{(2)}} |\vec{E}_1|^2 \vec{E}_1\, dx\, dy\right|^{2/3} \left|\int_{\chi^{(2)}} |\vec{E}_2|^2 \vec{E}_2\, dx\, dy\right|^{1/3}} \tag{4}$$

the calculated mode overlap factors for the 10th−12th TM modes are 5.02%, 1.62%, and 4.28%, respectively. By combining the phase-matching condition with the modal

https://doi.org/10.1021/acsphotonics.0c01785
ACS Photonics 2021, 8, 1344−1352

onverlap, higher SHG efficiency can be expected in 10th and 12th TM modes.

The experimentally identified second harmonic signals were recorded at 407 and 421 nm and are shown in Figure 4c. The MOCVD growth and the dry etching processes for the AlN waveguides may cause minor geometry discrepancy between the simulation and the experiment, which resulted in the small differences between the simulated and the experimentally recorded phase-matching points. Since the phase-matching wavelengths are dependent on the device geometry, the location of the SHG signal is invariant to pumping wavelengths, which is evident in Figure 4c. The d_{33} of AlN is ~45× higher than d_{31},[36] suggesting a higher efficiency when the fundamental mode is TM-polarized. The high SHG efficiency utilizing d_{33} was also observed from this work given in the Supporting Information.

Since the spectrum broadening is mainly contributed from the TE_{10} mode, the optical coherence of the broadband spectrum can be determined by evaluating the first-order coherence function of the TE_{10} mode:[9,13,16]

$$\left|g_{12}^{(1)}(\lambda)\right| = \left| \frac{\langle E_1^*(\lambda)E_2(\lambda)\rangle}{\sqrt{\langle |E_1(\lambda)|^2\rangle\langle |E_2(\lambda)|^2\rangle}} \right| \tag{5}$$

which is the ensemble average of multiple supercontinuum pulses. The simulation took 100 supercontinuum pulses with a standard shot noise at the input spectra, and the noise spectrum is constituted by one photon per spectral bin.[37] The simulated first-order coherence function of TE_{10} supercontinuum is shown in Figure 5a. In addition to shot noise, to emulate the intensity fluctuation of the pump source,[38,39] relative intensity noise (RIN) is also involved by applying amplitude variations to individual pulses, corresponding to the RIN in the frequency range of MHz. The obtained coherence function is depicted in Figure 5b at the amplitude fluctuation at 1% and 2%. A degradation of coherence is observed near the edge of the spectrum. Since the RIN level in MHz range is typically <1%,[40,41] the RIN is not critical to the coherence of the generated supercontinuum.

It should also be noted that the noise performance can be further investigated by involving phase jitter of the laser source[42] and the polarization modulation instability[39] as the crystalline structure of AlN is highly anisotropic, in which considerable birefringence is expected.[43]

CONCLUSION

In conclusion, we have demonstrated supercontinuum generation using a dispersion engineered AlN waveguide with ultralow input power. Notably, the main spectrum covers from 490 nm to over 1100 nm with a secondary SHG spectrum from 407 to 425 nm. Near-visible pumping was implemented to improve energy efficiency. To overcome the strong material dispersion, the AlN waveguides were designed to support high order modes. The experimental results were compared with the theoretical results from FDM and GMMNLS simulations. Further investigations on high order dispersion terms and propagation losses reveal that the SF process can only be initiated within a narrow window of waveguide width, which was supported by the experimental findings. The SHG spectrum was investigated by solving modal dispersions near 800 and 400 nm, and the corresponding phase-matching wavelengths were determined. Simulations of the first-order coherence function suggest that the spectrum broadening procedure is robust to noise. The outcome of our work demonstrates that the high order modes are experimentally applicable to efficient spectrum broadening and can greatly overcome the large material dispersion within the visible spectrum.

Noting that III−N material system exhibits excellent monolithic integration capability with lasers/detectors (InGaN) and high-speed RF transistors (AlGaN), the demonstration from this work is an important first step toward an on-chip fully integrated broadband supercontinuum source in the visible, which is of high interest in a range of fields including on-chip mode locking,[44] parametric oscillator,[45] and entangled photon generation.[46]

METHODS

Fabrication AlN Waveguides. The AlN thin films were coated with a ~600 nm SiO_2 layer using plasma-enhanced chemical vapor deposition (PECVD), followed by an 80 nm Cr layer using electron-beam evaporation. The two layers served as hardmasks for the dry etching processes. Photoresist ma-N 2403 was used to perform electron-beam lithography (EBL). The Cr layer was etched away using a user developed (chlorine + argon) reactive ion etching (RIE) process, while the SiO_2 layer was removed by standard anisotropic RIE etching process developed by ASU NanoFab. The AlN waveguide patterns were defined using a user developed inductively coupled plasma (ICP) etching with Cl_2, $BrCl_3$, and Ar chemistries at a bias voltage near 300 V. The waveguides were coated by 2 μm SiO_2 coating layers to reduce scattering loss. After fabrication, samples were cut and polished down to 0.1 μm grade. The fabricated waveguide has ~50 to 100 nm width variance due to the isotropic nature of the Cr etching process. This variance was included in numerical simulations. Detailed process flow and scanning electron microscope (SEM) images of the fabricated AlN waveguides can be found in Figure S2.

Simulation on Pulse Propagation. The pulse propagation along the waveguide was simulated using GMMNLS solved by split-step Fourier method,[26,47] where the fourth order Runge−Kutta method was also implemented to reduce computational load. The format of the GMMNLS used in this work was:

$$\begin{aligned}\frac{\partial A_p}{\partial z} = &-\frac{\alpha}{2}A_p + i\sum_{k\geq 2} i^k \frac{\beta_k}{k!}\frac{\partial^k A_p}{\partial t^k} + i\frac{n_2\omega_0}{c}\left(1 + \frac{i}{\omega_0}\frac{\partial}{\partial t}\right)\\ &\times \sum_{l\cdot m\cdot n}\left[(1-f_R)S^K_{plmn}A_lA_mA_n^* + f_R S^R_{plmn}A_l\int_{-\infty}^{t} d\tau h_R(\tau)\right.\\ &\left.\times A_m(z, t-\tau)A_n^*(z, t-\tau)\right]\end{aligned} \tag{6}$$

where $A_p(z, t)$ denotes the pulse slow varying amplitude of mode p, α is the propagation loss, β_k is the kth order dispersion, n_2 is the Kerr refractive index, f_R is the fraction of nonlinearity contributed from Raman response, and h_R is the Raman response function. The f_R was set to zero, as no significant red-shifted spectrum was observed through this whole study. The overlap factors S^R_{plmn} and S^K_{plmn} are

$$S^R_{plmn} = \frac{\int dx\ dy[\boldsymbol{F}_p^*\cdot\boldsymbol{F}_l][\boldsymbol{F}_m\cdot F_n^*]}{\left[\int dx\ dy|\boldsymbol{F}_p|^2\int dx\ dy|\boldsymbol{F}_l|^2\int dx\ dy|F_m|^2\int dx\ dy|\boldsymbol{F}_n|^2\right]^{1/2}} \tag{7}$$

https://doi.org/10.1021/acsphotonics.0c01785
ACS Photonics 2021, 8, 1344−1352

$$S^{K}_{plmn} = \frac{2}{3} S^{R}_{plmn} + \frac{1}{3} \frac{\int dx\ dy [\boldsymbol{F}^{*}_{p} \cdot \boldsymbol{F}^{*}_{n}][\boldsymbol{F}_{m} \cdot \boldsymbol{F}_{l}]}{\left[\int dx\ dy |\boldsymbol{F}_{p}|^{2} \int dx\ dy |\boldsymbol{F}_{l}|^{2} \int dx\ dy |\boldsymbol{F}_{m}|^{2} \int dx\ dy |\boldsymbol{F}_{n}|^{2}\right]^{1/2}} \quad (8)$$

the $\boldsymbol{F}_p$ indicates transverse mode profile. Dispersion terms were truncated at sixth order, but it is noteworthy that only third order dispersion plays significant role in modifying the spectrum. To estimate the Kerr refractive index of AlN, the experimental recorded data on n_2 at 1550 nm[48] was utilized by applying the wavelength-dependent fitting model,[49] n_2 at 800 nm can be estimated to be 2.5×10^{-19} m^2/W. The initial pulse shape was assumed to be Gaussian with a full-width-at-half-maximum (fwhm) of 100 fs. The propagation loss of TE_{10} mode is estimated to be ~20 dB/cm when waveguifde width is 1100−1200 nm.

High Order Mode Excitations. We adopted different waveguide excitation strategies in this work. The detailed description and an analysis of each excitation method is discussed in Figure S4. The most efficient excitation method was applying a normal taper with a ~5 μm taper width. Under low power operation, the beam was first focused at the center of taper, then the position was optimized by slowly varying the nanostage to move the focal point from the center to the edge of the taper facet. The out-scattered light was monitored by a CMOS camera at the same time. Since the TE_{10} mode has higher scattering loss comparing to the TE_{00} mode, when the out-scattered light reaches its maximum (as recorded by CMOS camera), the excitation efficiency of TE_{10} mode will be near its maximum. At this stage, the location of focusing point is near the edge of taper facet, which can be confirmed by the CMOS camera. An alternative way to excite the TE_{10} mode was to operate the system under higher power (near 30 mW on-chip average pumping power). By slowly varying the focal point from the center to the edge of the taper, DWs near 600 nm were generated due to the increasing excitation efficiency of the TE_{10} mode. The red radiation can be directly observed under a microscope, and the excitation efficiency of the TE_{10} mode can be optimized by maximizing the red radiation.

Estimation of Propagation Loss. The propagation losses of the TE_{00} modes were experimentally characterized by collecting out-scattered light along the propagation direction using a CMOS camera. The typical scattered optical power versus propagation length is provided in Figure S5. By adopting semilog plotting, the decay slope is proportional to the propagation loss of the TE_{00} mode in dB/cm. The low loss of the TE_{00} mode was further confirmed by measuring the intrinsic quality factor of ring resonators (Table S1).

The losses of TE_{00} modes with different waveguide widths were fitted by an in-house made dyadic Green's function (DGF) solver to obtain the sidewall roughness. The detailed description on DGF can be found in Supporting Information. DGF fitting gives sidewall roughness around 4 nm, which agrees well with standard optimized ICP etching process. By plugging in TE_{10} mode profile and sidewall roughness, the scattering loss can be estimated.

■ ASSOCIATED CONTENT

Supporting Information

The Supporting Information is available free of charge at https://pubs.acs.org/doi/10.1021/acsphotonics.0c01785.

Atomic force microscopy, ellipsometry, schematic of process flow, SEM images, propagation loss, estimation of propagation loss, laser-induced material damage, dyadic Green's function for loss estimation, and supplementary experimental data (PDF)

■ AUTHOR INFORMATION

Corresponding Authors

Yuji Zhao − *School of Electrical, Computer and Energy Engineering, Arizona State University, Tempe, Arizona 85287, United States*; Email: yuji.zhao@asu.edu

Andrea M. Armani − *Mork Family Department of Chemical Engineering and Materials Science, University of Southern California, Los Angeles, California 90089, United States*; orcid.org/0000-0001-9890-5104; Email: armani@usc.edu

Authors

Hong Chen − *School of Electrical, Computer and Energy Engineering, Arizona State University, Tempe, Arizona 85287, United States; Max Planck Institute of Microstructure Physics, Halle 06120, Germany*; orcid.org/0000-0003-4963-7515

Jingan Zhou − *School of Electrical, Computer and Energy Engineering, Arizona State University, Tempe, Arizona 85287, United States*

Dongying Li − *School of Electrical, Computer and Energy Engineering, Arizona State University, Tempe, Arizona 85287, United States*; orcid.org/0000-0003-3434-9924

Dongyu Chen − *Mork Family Department of Chemical Engineering and Materials Science, University of Southern California, Los Angeles, California 90089, United States*; orcid.org/0000-0001-8473-2804

Abhinav K. Vinod − *Department of Electrical Engineering, University of California, Los Angeles, California 90095, United States*

Houqiang Fu − *School of Electrical, Computer and Energy Engineering, Arizona State University, Tempe, Arizona 85287, United States; Department of Electrical and Computer Engineering, Iowa State University, Ames, Iowa 50011, United States*; orcid.org/0000-0002-1125-8328

Xuanqi Huang − *School of Electrical, Computer and Energy Engineering, Arizona State University, Tempe, Arizona 85287, United States*; orcid.org/0000-0002-7085-4162

Tsung-Han Yang − *School of Electrical, Computer and Energy Engineering, Arizona State University, Tempe, Arizona 85287, United States*

Jossue A. Montes − *School of Electrical, Computer and Energy Engineering, Arizona State University, Tempe, Arizona 85287, United States*

Kai Fu − *School of Electrical, Computer and Energy Engineering, Arizona State University, Tempe, Arizona 85287, United States*

Chen Yang − *School of Electrical, Computer and Energy Engineering, Arizona State University, Tempe, Arizona 85287, United States*

Cun-Zheng Ning − *School of Electrical, Computer and Energy Engineering, Arizona State University, Tempe, Arizona 85287, United States; Department of Electronic Engineering, Tsinghua University, Beijing 100084, China*

Chee Wei Wong − *Department of Electrical Engineering, University of California, Los Angeles, California 90095, United States*

Complete contact information is available at:
https://pubs.acs.org/10.1021/acsphotonics.0c01785

Author Contributions

The manuscript was written through contributions of all authors.

Notes

The authors declare no competing financial interest.

■ ACKNOWLEDGMENTS

This work was supported by the grant from Army Research Office (ARO) PECASE Grant No. W911NF-19-1-0089 and the ARO DURIP Grant No. W911NF-19-1-0129 monitored by Dr. Michael Gerhold. We gratefully acknowledge the use of facilities within the LeRoy Eyring Center for Solid State Science, ASU NanoFab, and ASU CLAS ultrafast laser facility. The authors would also like to thank Dr. Su Lin and Dr. Douglas Daniel for their great assistance in the early state of this research.

■ REFERENCES

(1) Schawlow, A. L.; Townes, C. H. Infrared and optical masers. *Phys. Rev.* **1958**, *112* (6), 1940.
(2) Maiman, T. H. Stimulated optical radiation in ruby. *Nature* **1960**, *187* (4736), 493−494.
(3) Fan, F.; Turkdogan, S.; Liu, Z.; Shelhammer, D.; Ning, C. Z. A monolithic white laser. *Nat. Nanotechnol.* **2015**, *10* (9), 796.
(4) Rosemann, N. W.; Eußner, J. P.; Beyer, A.; Koch, S. W.; Volz, K.; Dehnen, S.; Chatterjee, S. A highly efficient directional molecular white-light emitter driven by a continuous-wave laser diode. *Science* **2016**, *352* (6291), 1301−1304.
(5) Udem, T.; Holzwarth, R.; Hänsch, T. W. Optical frequency metrology. *Nature* **2002**, *416* (6877), 233−237.
(6) Rosenband, T.; Hume, D. B.; Schmidt, P. O.; Chou, C. W.; Brusch, A.; Lorini, L.; Oskay, W. H.; Drullinger, R. E.; Fortier, T. M.; Stalnaker, J. E.; Diddams, S. A.; Swann, W. C.; Newbury, N. R.; Itano, W. M.; Wineland, D. J.; Bergquist, J. C. Frequency ratio of Al^+ and Hg^+ single-ion optical clocks; metrology at the 17th decimal place. *Science* **2008**, *319* (5871), 1808−1812.
(7) Tu, H.; Boppart, S. A. Coherent fiber supercontinuum for biophotonics. *Laser Photonics Rev.* **2013**, *7* (5), 628−645.
(8) Humbert, G.; Wadsworth, W. J.; Leon-Saval, S. G.; Knight, J. C.; Birks, T. A.; Russell, P. S. J.; Lederer, M. J.; Kopf, D.; Wiesauer, K.; Breuer, E. I.; Stifter, D. Supercontinuum generation system for optical coherence tomography based on tapered photonic crystal fibre. *Opt. Express* **2006**, *14* (4), 1596−1603.
(9) Kuyken, B.; Ideguchi, T.; Holzner, S.; Yan, M.; Hansch, T. W.; Van Campenhout, J.; Verheyen, P.; Coen, S.; Leo, F.; Baets, R.; Roelkens, G.; Picque, N. An octave-spanning mid-infrared frequency comb generated in a silicon nanophotonic wire waveguide. *Nat. Commun.* **2015**, *6* (1), 1−6.
(10) Singh, N.; Xin, M.; Vermeulen, D.; Shtyrkova, K.; Li, N.; Callahan, P. T; Magden, E. S.; Ruocco, A.; Fahrenkopf, N.; Baiocco, C.; Kuo, B. P-P; Radic, S.; Ippen, E.; Kartner, F. X; Watts, M. R Octave-spanning coherent supercontinuum generation in silicon on insulator from 1.06 μm to beyond 2.4 μm. *Light: Sci. Appl.* **2018**, *7* (1), 17131−17131.
(11) Dave, U. D.; Ciret, C.; Gorza, S. P.; Combrie, S.; De Rossi, A.; Raineri, F.; Roelkens, G.; Kuyken, B. Dispersive-wave-based octave-spanning supercontinuum generation in InGaP membrane waveguides on a silicon substrate. *Opt. Lett.* **2015**, *40* (15), 3584−3587.
(12) Oh, D. Y.; Yang, K. Y.; Fredrick, C.; Ycas, G.; Diddams, S. A.; Vahala, K. J. Coherent ultra-violet to near-infrared generation in silica ridge waveguides. *Nat. Commun.* **2017**, *8* (1), 1−7.
(13) Guo, H.; Herkommer, C.; Billat, A.; Grassani, D.; Zhang, C.; Pfeiffer, M. H.; Weng, W.; Bres, C. S.; Kippenberg, T. J. Mid-infrared frequency comb via coherent dispersive wave generation in silicon nitride nanophotonic waveguides. *Nat. Photonics* **2018**, *12* (6), 330−335.
(14) Zhang, L.; Yan, Y.; Yue, Y.; Lin, Q.; Painter, O.; Beausoleil, R. G.; Willner, A. E. On-chip two-octave supercontinuum generation by enhancing self-steepening of optical pulses. *Opt. Express* **2011**, *19* (12), 11584−11590.
(15) Chen, B. Q.; Zhang, C.; Hu, C. Y.; Liu, R. J.; Li, Z. Y. High-efficiency broadband high-harmonic generation from a single quasi-phase-matching nonlinear crystal. *Phys. Rev. Lett.* **2015**, *115* (8), 083902.
(16) Hickstein, D. D.; Jung, H.; Carlson, D. R.; Lind, A.; Coddington, I.; Srinivasan, K.; Ycas, G. G.; Cole, D. C.; Kowligy, A.; Fredrick, C.; Droste, S.; Lamb, E. S.; Newbury, N. R.; Tang, H. X.; Diddams, S. A.; Papp, S. B. Ultrabroadband supercontinuum generation and frequency-comb stabilization using on-chip waveguides with both cubic and quadratic nonlinearities. *Phys. Rev. Appl.* **2017**, *8* (1), 014025.
(17) Liu, X.; Bruch, A. W.; Lu, J.; Gong, Z.; Surya, J. B.; Zhang, L.; Wang, J.; Yan, J.; Tang, H. X. Beyond 100 THz-spanning ultraviolet frequency combs in a non-centrosymmetric crystalline waveguide. *Nat. Commun.* **2019**, *10* (1), 1−8.
(18) Stark, S. P.; Travers, J. C.; Russell, P. S. J. Extreme supercontinuum generation to the deep UV. *Opt. Lett.* **2012**, *37* (5), 770−772.
(19) Jiang, X.; Joly, N. Y.; Finger, M. A.; Babic, F.; Wong, G. K.; Travers, J. C.; Russell, P. S. J. Deep-ultraviolet to mid-infrared supercontinuum generated in solid-core ZBLAN photonic crystal fibre. *Nat. Photonics* **2015**, *9* (2), 133−139.
(20) Johnson, A. R.; Mayer, A. S.; Klenner, A.; Luke, K.; Lamb, E. S.; Lamont, M. R. E.; Joshi, C.; Okawachi, Y.; Wise, F. W.; Lipson, M.; Keller, U.; Gaeta, A. L. Octave-spanning coherent supercontinuum generation in a silicon nitride waveguide. *Opt. Lett.* **2015**, *40* (21), 5117−5120.
(21) Lu, J.; Liu, X.; Bruch, A. W.; Zhang, L.; Wang, J.; Yan, J.; Tang, H. X. Ultraviolet to mid-infrared supercontinuum generation in single-crystalline aluminum nitride waveguides. *Opt. Lett.* **2020**, *45* (16), 4499−4502.
(22) Niffenegger, R. J.; Stuart, J.; Sorace-Agaskar, C.; Kharas, D.; Bramhavar, S.; Bruzewicz, C. D.; Loh, W.; Maxson, R. T.; McConnell, R.; Reens, D.; West, G. N.; Sage, J. M.; Chiaverini, J. Integrated multi-wavelength control of an ion qubit. *Nature* **2020**, *586* (7830), 538−542.
(23) Mohanty, A.; Li, Q.; Tadayon, M. A.; Roberts, S. P.; Bhatt, G. R.; Shim, E.; Ji, X.; Cardenas, J.; Miller, S. A.; Kepecs, A.; Lipson, M. Reconfigurable nanophotonic silicon probes for sub-millisecond deep-brain optical stimulation. *Nat. Biome. Eng.* **2020**, *4* (2), 223−231.
(24) Boyraz, O.; Indukuri, T.; Jalali, B. Self-phase-modulation induced spectral broadening in silicon waveguides. *Opt. Express* **2004**, *12* (5), 829−834.
(25) Del'Haye, P.; Schliesser, A.; Arcizet, O.; Wilken, T.; Holzwarth, R.; Kippenberg, T. J. Optical frequency comb generation from a monolithic microresonator. *Nature* **2007**, *450* (7173), 1214−1217.
(26) Agrawal, G. P. *Nonlinear Fiber Optics*; Springer: Berlin, Heidelberg, 2000, p 602.
(27) Fallahkhair, A. B.; Li, K. S.; Murphy, T. E. Vector finite difference modesolver for anisotropic dielectric waveguides. *J. Lightwave Technol.* **2008**, *26* (11), 1423−1431.
(28) Ji, X.; Barbosa, F. A.; Roberts, S. P.; Dutt, A.; Cardenas, J.; Okawachi, Y.; Bryant, A.; Gaeta, A. L.; Lipson, M. Ultra-low-loss on-chip resonators with sub-milliwatt parametric oscillation threshold. *Optica* **2017**, *4* (6), 619−624.
(29) Watanabe, N.; Kimoto, T.; Suda, J. Thermo-optic coefficients of 4H-SiC, GaN, and AlN for ultraviolet to infrared regions up to 500° C. *Jpn. J. Appl. Phys.* **2012**, *51* (11R), 112101.
(30) Ciret, C.; Gorza, S. P.; Husko, C.; Roelkens, G.; Kuyken, B.; Leo, F. Physical origin of higher-order soliton fission in nanophotonic semiconductor waveguides. *Sci. Rep.* **2018**, *8* (1), 1−11.
(31) Foster, M. A.; Dudley, J. M.; Kibler, B.; Cao, Q.; Lee, D.; Trebino, R.; Gaeta, A. L. Nonlinear pulse propagation and

supercontinuum generation in photonic nanowires: experiment and simulation. *Appl. Phys. B: Lasers Opt.* **2005**, *81* (2−3), 363−367.
(32) Kibler, B.; Dudley, J. M.; Coen, S. Supercontinuum generation and nonlinear pulse propagation in photonic crystal fiber: influence of the frequency-dependent effective mode area. *Appl. Phys. B: Lasers Opt.* **2005**, *81* (2−3), 337−342.
(33) Yang, Q. F.; Yi, X.; Yang, K. Y.; Vahala, K. Spatial-mode-interaction-induced dispersive waves and their active tuning in microresonators. *Optica* **2016**, *3* (10), 1132−1135.
(34) Liu, G.; Yan, C.; Zhou, G.; Wen, J.; Qin, Z.; Zhou, Q.; Li, B.; Zheng, R.; Wu, H.; Sun, Z. Broadband white-light emission from alumina nitride bulk single crystals. *ACS Photonics* **2018**, *5* (10), 4009−4013.
(35) Luo, R.; He, Y.; Liang, H.; Li, M.; Lin, Q. Highly tunable efficient second-harmonic generation in a lithium niobate nanophotonic waveguide. *Optica* **2018**, *5* (8), 1006−1011.
(36) Majkić, A.; Franke, A.; Kirste, R.; Schlesser, R.; Collazo, R.; Sitar, Z.; Zgonik, M. Optical nonlinear and electro-optical coefficients in bulk aluminium nitride single crystals. *Phys. Status Solidi B* **2017**, *254* (9), 1700077.
(37) Dudley, J. M.; Coen, S. Numerical simulations and coherence properties of supercontinuum generation in photonic crystal and tapered optical fibers. *IEEE J. Sel. Top. Quantum Electron.* **2002**, *8* (3), 651−659.
(38) Rao, S.; Engelsholm, R. D.; Gonzalo, I. B.; Zhou, B.; Bowen, P.; Moselund, P. M.; Bang, O.; Bache, M. Ultra-low-noise supercontinuum generation with a flat near-zero normal dispersion fiber. *Opt. Lett.* **2019**, *44* (9), 2216−2219.
(39) Gonzalo, I. B.; Engelsholm, R. D.; Sørensen, M. P.; Bang, O. Polarization noise places severe constraints on coherence of all-normal dispersion femtosecond supercontinuum generation. *Sci. Rep.* **2018**, *8* (1), 1−13.
(40) Gürel, K.; Wittwer, V. J.; Hakobyan, S.; Schilt, S.; Südmeyer, T. Carrier envelope offset frequency detection and stabilization of a diode-pumped mode-locked Ti: sapphire laser. *Opt. Lett.* **2017**, *42* (6), 1035−1038.
(41) Vernaleken, A.; Schmidt, B.; Wolferstetter, M.; Hänsch, T. W.; Holzwarth, R.; Hommelhoff, P. Carrier-envelope frequency stabilization of a Ti: sapphire oscillator using different pump lasers. *Opt. Express* **2012**, *20* (16), 18387−18396.
(42) Vernaleken, A.; Schmidt, B.; Wolferstetter, M.; Hänsch, T. W.; Holzwarth, R.; Hommelhoff, P. Carrier-envelope frequency stabilization of a Ti: sapphire oscillator using different pump lasers. *Opt. Express* **2012**, *20* (16), 18387−18396.
(43) Rigler, M.; Buh, J.; Hoffmann, M. P.; Kirste, R.; Bobea, M.; Mita, S.; Gerhold, M. D.; Collazo, R.; Sitar, Z.; Zgonik, M. Optical characterization of Al-and N-polar AlN waveguides for integrated optics. *Appl. Phys. Express* **2015**, *8* (4), 042603.
(44) Koch, B. R.; Fang, A. W.; Cohen, O.; Bowers, J. E. Mode-locked silicon evanescent lasers. *Opt. Express* **2007**, *15* (18), 11225−11233.
(45) Levy, J. S.; Gondarenko, A.; Foster, M. A.; Turner-Foster, A. C.; Gaeta, A. L.; Lipson, M. CMOS-compatible multiple-wavelength oscillator for on-chip optical interconnects. *Nat. Photonics* **2010**, *4* (1), 37−40.
(46) Kues, M.; Reimer, C.; Roztocki, P.; Cortes, L. R.; Sciara, S.; Wetzel, B.; Zhang, Y.; Cino, A.; Chu, S. T.; Little, B. E.; Moss, D. J.; Caspani, L.; Azana, J.; Morandotti, R. On-chip generation of high-dimensional entangled quantum states and their coherent control. *Nature* **2017**, *546* (7660), 622−626.
(47) Horak, P.; Poletti, F. Multimode nonlinear fibre optics: Theory and applications. *Recent Progress in Optical Fiber Research* **2012**, 3−25.
(48) Jung, H.; Xiong, C.; Fong, K. Y.; Zhang, X.; Tang, H. X. Optical frequency comb generation from aluminum nitride microring resonator. *Opt. Lett.* **2013**, *38* (15), 2810−2813.
(49) Sheik-Bahae, M.; Hutchings, D. C.; Hagan, D. J.; Van Stryland, E. W. Dispersion of bound electron nonlinear refraction in solids. *IEEE J. Quantum Electron.* **1991**, *27* (6), 1296−1309.

https://doi.org/10.1021/acsphotonics.0c01785
ACS Photonics 2021, 8, 1344−1352